

# Dawn-dusk asymmetry in the main auroral emissions at Jupiter observed with Juno-UVS

A Groulard<sup>1</sup>, Bertrand Bonfond<sup>1</sup>, D Grodent<sup>1</sup>, J.-C Gérard<sup>1</sup>, T K Greathouse<sup>2</sup>, V Hue<sup>3</sup>, G R Gladstone<sup>2</sup>, and M H Versteeg<sup>2</sup>

<sup>1</sup>Laboratory for Planetary and Atmospheric Physics, Space Sciences, Technologies and Astrophysical Research Institute, University of Liège

<sup>2</sup>Southwest Research Institute

<sup>3</sup>Institut Origines, LAM, Aix-Marseille Université, CNRS, CNES

January 16, 2024

## Abstract

Jupiter's main auroral emissions usually form auroral curtains surrounding the magnetic poles. Most explanations for this auroral feature are based on corotation enforcement currents flowing between the magnetosphere and the ionosphere. This process predicts the highest emitted power to originate from the dawn region, while the lowest emitted power would come from the noon to dusk region. However, a previous study using Hubble Space Telescope data showed the opposite, with a higher emitted power in the dusk region in the south and ambiguous results in the north. In the present study, we use data from the first 39 Juno perijoves to reexamine this question. We find a dusk region 3.3 to 5.5 times more powerful than the dawn one, in qualitative agreement with the previous study but contrary to theoretical expectations. These results support the idea that the main emissions cannot be fully described by corotation enforcement currents.

1 **Dawn-dusk asymmetry in the main auroral emissions at Jupiter**  
2 **observed with Juno-UVS**

3

4 A. Groulard<sup>1</sup>, B. Bonfond<sup>1\*</sup>, D. Grodent<sup>1</sup>, J.-C. Gérard<sup>1</sup>, T. K. Greathouse<sup>2</sup>, V. Hue<sup>3</sup>, G. R.  
5 Gladstone<sup>2</sup>, M. H. Versteeg<sup>2</sup>

6 \*Corresponding author: b.bonfond@uliege.be

7 <sup>1</sup>Laboratory for Planetary and Atmospheric Physics, Space Sciences, Technologies and  
8 Astrophysical Research Institute, University of Liège, Liège, Belgium

9 <sup>2</sup>Southwest Research Institute, San Antonio, TX, USA

10 <sup>3</sup>Aix-Marseille Université, CNRS, CNES, Institut Origines, LAM, Marseille, France

11

12 **0 | Abstract**

13

14 Jupiter's main auroral emissions usually form auroral curtains surrounding the magnetic  
15 poles. Most explanations for this auroral feature are based on corotation enforcement  
16 currents flowing between the magnetosphere and the ionosphere. This process predicts the  
17 highest emitted power to originate from the dawn region, while the lowest emitted power  
18 would come from the noon to dusk region. However, a previous study using Hubble Space  
19 Telescope data showed the opposite, with a higher emitted power in the dusk region in the  
20 south and ambiguous results in the north. In the present study, we use data from the first 39  
21 Juno perijoves to reexamine this question. We find a dusk region 3.3 to 5.5 times more  
22 powerful than the dawn one, in qualitative agreement with the previous study but contrary  
23 to theoretical expectations. These results support the idea that the main emissions cannot be  
24 fully described by corotation enforcement currents.

25

## 26 **1 | Introduction**

27

28 The UV aurorae at Jupiter are made of various structures having different origins (see e.g. the  
29 review in Grodent, 2015). The main emissions are the most easily identifiable of them. They  
30 generally take the shape of an almost closed curtain centered on the jovimagnetic poles (the  
31 intersections of the magnetic dipole axis with the surface), with a systematic brightness  
32 decrease between 10:00 and 12:00 magnetic local time (Radioti et al., 2008). In the southern  
33 hemisphere, the nearly dipolar field gives an oval shape to the main emissions, while a  
34 magnetic anomaly related to the high order terms of the magnetic field multipolar  
35 development gives them a bean shape in the northern hemisphere (Grodent et al., 2008;  
36 Connerney et al., 2022). The persistence of this main component of the aurorae is presumably  
37 due to its formation mechanism.

38

39 The most widely accepted explanation for the main auroral emissions at Jupiter before the  
40 Juno era was related to the magnetosphere-ionosphere coupling current system enforcing  
41 the partial corotation of the plasma in the Jovian middle magnetosphere (Cowley and Bunce,  
42 2001; Hill, 2001). When particles produced by the volcanically active moon Io are ionized, they  
43 end up forming a plasma torus around Jupiter, corotating with the planet along the moon's  
44 orbit. Because of a balance between centrifugal, thermal and Lorentz forces, the plasma in  
45 the torus progressively diffuses radially outward into a plasmashet. A corotation  
46 enforcement current loop arises to maintain the corotation of the plasma, transferring  
47 angular momentum from Jupiter's polar atmosphere to the magnetosphere. In the equatorial  
48 plane of the magnetosphere, this current flows radially, which manifests as an azimuthal

49 bendback of the magnetic field lines. It then flows along magnetic field lines and closes in the  
50 ionosphere via Pedersen currents. As the iogenic plasma moves further away from the planet,  
51 the upward (relative to Jupiter) field aligned currents (FACs) enforce a significant degree of  
52 corotation (~75-90% of full corotation) up to around 20-40  $R_J$  before the plasma's angular  
53 velocity starts to drop significantly at larger distances. The field aligned currents peak in this  
54 transition region where the corotation breaks down. According to this family of models, such  
55 upward FACs accelerate electrons towards Jupiter's atmosphere via quasi-static electric  
56 fields, generating the main auroral emissions at the feet of the field lines. The main emissions  
57 magnetically map to distances between 15 and 60 Jupiter radii ( $R_J$ ) in the magnetosphere  
58 (Vogt et al., 2011), similarly to estimated magnetospheric roots of the field aligned current  
59 sheets observed by Juno (Kamran et al., 2022). This theory provides a straightforward  
60 explanation for the persistence of the main emissions over long timescales and for the  
61 existence of the field aligned currents inferred from magnetic field measurements (Kamran  
62 et al., 2022; Kotsiaros et al., 2019; Nichols and Cowley, 2022; Sulaiman et al., 2022). However,  
63 Bonfond et al., (2020) have questioned this simplified picture recently after highlighting an  
64 increasing number of observations which appear in contradiction with the model's  
65 expectations. For example, as the magnetic field topology and plasma flow are not uniform  
66 around the planet, Ray et al. (2014) used a 1-D model based on this theory to predict how the  
67 intensity of the main emission varies over local times. According to this model, the strongest  
68 aurorae should take place at dawn and should be at least one order of magnitude stronger  
69 than in the dusk region. . This prediction has been tested by Bonfond et al. (2015) , who used  
70 Hubble Space Telescope (HST) data to determine and compare the power emitted in the dusk  
71 and dawn parts of the main emissions. They found a dusk region about 3 times more powerful  
72 than the dawn one in the southern hemisphere, which is in disagreement with the Ray et al.

73 (2014) model. They also have found that both regions were equally powerful in the northern  
74 hemisphere. However, they noted that the later results should be considered with caution.  
75 Indeed, the HST observations are hampered by the telescope's viewing geometry, which is  
76 such that HST cannot observe the night side aurora and most images are acquired when the  
77 jovimagnetic pole of interest is tilted towards the Earth. This issue is more prominent in the  
78 north since the barycenter of the main auroral emission is located at lower latitude. This  
79 limitation is further magnified by the presence of a large magnetic anomaly near 100° System  
80 III longitude. System III is the longitude system fixed with Jupiter's magnetic field extensively  
81 used to study the magnetic phenomena taking place at Jupiter. Based on their results in the  
82 southern hemisphere, which they considered more reliable, the authors concluded that the  
83 main emissions cannot be fully described by the theory of partial corotation enforcement in  
84 the middle magnetosphere. The partial ring current observed at Jupiter (Khurana, 2001) has  
85 been suggested to generate FACs increasing the emitted power in the dusk region, and  
86 lowering it in the dawn region, to explain the disagreement between their results and the  
87 model. The purpose of the present study is to further constrain the findings of Bonfond et al.  
88 (2015) with observations unaffected by Earth orbit viewing geometry.

89

90 The morphology and intensity of the main emissions may also vary over a few hours. For  
91 example, instead of a simple and well defined arc, the main emissions sometimes appear to  
92 form forks and parallel arcs, and patchy features can be seen from time to time (Nichols et  
93 al., 2009). In addition to these disturbances, two kinds of events can increase the emitted  
94 power of the aurorae (Yao et al., 2022): dawn storms and main auroral brightenings. Bonfond  
95 et al. (2021) have found dawn storms in about half of the first 20 Juno perijoves (PJ). They

96 also extended the definition of these storms to a chain of events lasting from 5 to 10 hours,  
97 ending with 1 to 2 hours of intense brightening of the dawn region of the main emissions. A  
98 more global brightening coupled with a shrinking of the main emission can also occur during  
99 solar wind compressions of the magnetosphere (Nichols et al., 2007, 2009, 2017; Yao et al.,  
100 2022).

101 The discrepancy between the dawn/dusk auroral power ratio in the northern and southern  
102 hemispheres based on the HST data called for a re-investigation of this problem with unbiased  
103 data. Here we carry out a similar study, based on UV auroral observations carried out with  
104 the Ultraviolet Spectrograph on board the Juno spacecraft.

105

## 106 **2| Observations**

107

108 The NASA Juno spacecraft arrived at Jupiter on July 5th, 2016 (Bolton et al., 2017). It was  
109 placed in a highly eccentric polar orbit bringing it to an altitude of only 4000 km at its periapsis,  
110 and out to 8 million km near apoapsis well out into the magnetosphere. This orbit offers the  
111 advantage of gathering high resolution data of Jupiter, while being able to study the whole  
112 environment of the planet. Juno is a spinning spacecraft, undergoing one rotation every 30 s.  
113 It carries 10 scientific instruments, including a longslit UltraViolet Spectrograph (UVS) used in  
114 this study. UVS is a photon-counting imaging spectrograph operating in the 68-210 nm range  
115 (Gladstone et al., 2017). The UVS field of view consists of a 7.2° long slit divided into three  
116 parts. The 2 external parts are 0.2° wide, while the central one is narrower and has a width of  
117 only 0.025°. Individual photons are counted and calibrated using the effective area derived

118 from many stellar observations (Hue et al., 2019), while the wavelength registration comes  
119 from pre-launch measurements (Davis et al., 2011; Hue et al., 2021). As they provide a higher  
120 signal-to-noise ratio, only the external wider parts of the slit were used in this study. The data  
121 used for this study are selected among the observations acquired with Juno-UVS during four  
122 hours in each hemisphere when the spacecraft flies over the poles close to its perijove.

123

124 We first created polar brightness maps of the aurorae in the same way as described by  
125 Bonfond et al. (2021). Specifically, after removing the noise from the images, data gathered  
126 over 100 spins of the spacecraft were added and weighted to build the final map. This method  
127 has the advantage of allowing the creation of comprehensive maps of the aurorae for most  
128 of the perijoves, but the tradeoff is a long (~50 minutes) time interval between the first and  
129 the last spins. This process was repeated for the first 39 perijoves of Juno in both hemispheres.  
130 Because of the limited coverage of the poles by Juno during some perijoves, only 63 maps  
131 were considered in the study. More precisely, out of the 39 possible maps for each perijove,  
132 38 were kept in the southern hemisphere and 25 in the northern hemisphere. The detailed  
133 times of observation for each perijove can be found in the supplementary material. In this  
134 study, we only considered the time intervals during which the high voltage was nominal. The  
135 indicated brightness is the total FUV brightness emitted by H<sub>2</sub> in kR units. In order to mitigate  
136 the effect of hydrocarbon absorption (especially methane, below 140 nm), we first only  
137 considered the unabsorbed 145-165 nm wavelength range and then multiplied it by a factor  
138 of 4.4 to extend the brightness to the whole FUV H<sub>2</sub> spectrum. To account for the fact that  
139 the assumed emitting surface is not perpendicular to the viewing axis, we multiplied the  
140 observed brightness by the cosine of the local emission angle, which typically lies around ~30-

141 40°. To derive the emitted power, we multiply the brightness by the mean photon energy  
142 ( $1.65 \cdot 10^{-18}$  J) and by the emission surface in the region of interest.

143

### 144 **3 | Analysis**

145

146 While the main emissions clearly stand out when co-adding many UV auroral images,  
147 identifying them on individual images can become tricky when the morphology becomes  
148 complex (parallel arc, dawn storms, etc.). In order to get robust results, we decided to use 3  
149 different methods to build masks isolating the main emissions and we used 2 different  
150 definitions of the dawn and dusk sectors. First, since the size of the main auroral oval varies  
151 with time, we used a pair of “generic” masks, one for a contracted auroral oval and one for  
152 an expanded auroral oval, using the one most appropriate for the case under study. This  
153 method is somewhat similar to the one used by Bonfond et al. (2015), who used monthly  
154 averaged reference ovals to build masks and then used this mask for all images during that  
155 month. Then we built “adjusted” masks, fitting the location of the main emissions as closely  
156 as possible for each individual image, but with a constant width. We then built masks by fitting  
157 both the location and the width.

158

#### 159 **3.1 | Main emissions masks**

160

161 The first mask built to isolate the main emissions, the Magnetospheric Distance mask (MD  
162 mask), was created based on the Vogt et al. (2011) magnetic mapping model. It is thought to

163 be more reliable than models based on the combination of an internal field and a current  
164 disk in the middle magnetosphere, which is the region where the plasma that feeds the main  
165 emissions is located. Indeed, it accounts for the influence of local time on the magnetic field  
166 and it is rooted on measurements of the Ganymede footprint path from the Hubble Space  
167 Telescope and of magnetic flux in the equatorial plane from Galileo. Using this model, two  
168 masks were created to cover locations mapping to a constant distance of 30 and 40  $R_J$  in the  
169 magnetosphere to take into account the variable location of the main emissions. Indeed, as  
170 already mentioned, Vogt et al. (2011) have found the main emission to map between 15 and  
171 60  $R_J$  in the magnetosphere. We chose distances of 30 and 40  $R_J$  as it is in the middle of this  
172 interval so that we have better chances of covering the main emissions well. To do so, we  
173 chose 36 equally spaced local times. Those are used to find the longitude and latitude of the  
174 ionospheric locations mapping to these local times at a distance of 30 and 40  $R_J$  in the  
175 magnetosphere based on the Vogt et al. (2011) model. These ionospheric locations have then  
176 been interpolated to obtain ribbons covering all longitudes. At each point constituting the  
177 ribbons, the widths of the ribbons have then been extended to  $2^\circ$  in the direction of the axis  
178 linking that point to the barycenter of the aurorae, so that the masks overlap most of the  
179 main auroral emissions without including contributions from other auroral features. As the  
180 main emissions morphology changes over time, the location of its barycenter can also slightly  
181 move. Still, in this study we assumed the barycenter to be located at  $73.9^\circ$  latitude and  $185.6^\circ$   
182 System III longitude in the north; and  $-81.9^\circ$  latitude and  $31.9^\circ$  System III longitude in the  
183 south since its exact location does not have a marked impact on our results. These locations  
184 have been derived from images coming from the 2007 HST campaign. To choose between the  
185 contracted oval mask and the expanded oval mask, we computed the total power in the area  
186 covered by both masks. The mask with the largest total power was kept as the MD mask

187 (Figure 1, panel 2a), while the other one was discarded. In order to be able to select sub-  
188 elements of this mask corresponding to the different local time sectors, our masks are not  
189 just binary masks, but each element of the mask is attributed a value related to the angle  
190 centered on the barycenter of the aurorae (Figure 1, panel 2b).

191

192 The two other masks were created based on the actual location of the MEs in the images.  
193 Because arcs can be present not only in the MEs, but also on the polar region and in the  
194 equatorward emissions, we must exclude these regions from our search and focus on the  
195 region where they are the most likely to appear. To do so, we decided to use as a first guess  
196 the suite of masks based on the 2007 HST campaign (Bonfond et al., 2012; Clarke et al.,  
197 2009)The HST mask with the best overlap of the main emission was chosen as a starting point.  
198 For each tenth of a degree of longitude, the brightness peak was searched in the surrounding  
199 of the HST mask, assuming this peak is due to the main emissions. The HST mask has  
200 essentially been used to restrict the search area and make sure to discard the IFP which can  
201 be brighter than the main emissions in some locations. For areas where the main emissions  
202 are fainter than usual, the highest gradient of brightness was searched instead of the highest  
203 brightness. Indeed, based on the idea that the main emissions are associated with FACs due  
204 to corotation enforcement, they should correspond to an auroral curtain with a higher peak  
205 brightness than its surrounding, and a high gradient of brightness should be present at its  
206 edges. Once done for all the longitudes of interest, a Fourier series was fitted to the locations  
207 thus found. This method results in a smooth ribbon at the center of the main emissions. As  
208 for the MD mask, the ribbon was extended to be  $2^\circ$  wide to cover the whole width of the main  
209 emissions. An example of such an AF1 mask over the aurorae can be seen in Figure 1, panel

210 3a. The mask also has different values for different angles around the barycenter of the  
211 aurorae for later considerations (Figure 1, panel 3b).

212

213 The last mask is the Auroral Fit with variable width mask (AF2 mask). It has been created to  
214 take into account the complex shape that the main emissions can take during some perijoves.  
215 When the main emissions are composed of parallel arcs or unusual particularly wide features,  
216 it can be more extended than  $2^\circ$ . Thus, the two first masks may be too narrow in several  
217 places, and a third one is needed to more accurately deal with these unusual cases. To create  
218 the AF2 mask, we started from the boundaries of the AF1 mask. To find broad auroral main  
219 emissions, we looked for high brightness regions partly covered by the AF1 mask. To do so,  
220 we used a brightness threshold defined based on the brightness of the area covered by the  
221 AF1 mask for each tenth of degree around the barycenter. If there are emissions above that  
222 threshold just outside the AF1 mask, they are considered as part of the main emissions and  
223 they must be covered by the mask. In this case, new limits are defined to encompass them. If  
224 there is no such bright region, the AF1 limits are kept. After that, the new inner and outer  
225 limits have been fitted independently with Fourier series, so that it gives two ribbons that  
226 serve as the limits of the AF2 mask. This way, the mask is at least  $2^\circ$  wide in latitude, but can  
227 be broader if the main emissions are more extended at some locations (Figure 1, panel 4a).  
228 As for the two other masks, the value of the different points of the mask is linked to its angle  
229 around the barycenter of the aurorae (Figure 1, panel 4b). This mask is a generalized version  
230 of the AF1 mask. It has been needed for 27 of the 63 maps, since its usefulness relies on an  
231 unusual shape of the main emissions. Out of them, 8 are in the northern hemisphere, and 19

232 in the southern one. Even for these maps, the broadening of the mask is not necessarily in  
233 the dusk or dawn region, and the AF2 mask only has an impact on few perijoves.

234

### 235 **3.2 | Dawn and dusk regions selection**

236

237 Two different local time extents of the dusk and dawn regions in the magnetosphere were  
238 selected to study the emitted power. The first one, the B15 sector, ranges from 16:00 to 18:00  
239 LT in the dusk region, and from 06:00 to 08:00 LT in the dawn region. Its size was set to match  
240 the study performed by Bonfond et al. (2015) in order to compare our results to theirs. The  
241 second one, the SYM sector, ranges from 16:00 LT to 20:00 LT in the dusk region, and from  
242 04:00 LT to 08:00 LT in the dawn one. This sector is symmetrical over the dusk local time (i.e.:  
243 18:00 LT) and the dawn local time (i.e.: 06:00 LT), which is a more natural choice to study  
244 these regions. This sector could not be studied with HST due to its orbit that did not allow for  
245 a view of the night part of the planet.

246

247 We used the Vogt et al. (2011) magnetic mapping model, with the JRM09 model (Connerney  
248 et al., 2018) as input magnetic field model, to link the desired local times in the  
249 magnetosphere to locations in the ionosphere. Each magnetospheric local time corresponds  
250 to a given angle relative to the barycenter of the aurorae in the ionosphere. The model  
251 provides a longitude-latitude location in the ionosphere from a location with a known  
252 longitude and distance in the magnetosphere. The desired local times are used as the input  
253 longitude, and a distance of  $30 R_J$  is used as the input distance since it is expected to map to

254 the main emissions. All the ionospheric longitude-latitude coordinates can then be  
255 transformed into polar coordinates. Thanks to the way the three masks were created, with  
256 the value of a location proportional to its angle around the barycenter (Figures 1, panels b),  
257 one can easily find the different sectors in the ionosphere from the locations expressed in  
258 polar coordinates. This way, we have limited the main emissions masks to the two sectors of  
259 interest to study the emitted power from the two regions.

260 The maps that could not be used at all because the aurorae were not well imaged have already  
261 been ruled out of the study, but additional problems arise. Some UVS auroral maps are  
262 incomplete in a part of the dusk or dawn region, and the main emissions mask is not  
263 accurately placed in others. The second case mostly happens for the MD mask, which maps  
264 to a constant distance in the magnetosphere, while the origin of the main emissions is at a  
265 variable distance (see the example of PJ12 north in the supplemental material). Bonfond et  
266 al. (2015) had already noted that in some rare cases, their generic monthly oval would  
267 completely miss the aurora on one side (generally the dusk one). Because these cases are  
268 both rare and lead to obviously erroneous results, the study has been restricted to 338 sectors  
269 out of the 378 possible sectors of the 63 maps.

270

## 271 **4| Results and discussion**

272

273 For each sector, the dusk-over-dawn power ratio was computed, and the results can be seen  
274 in Figure 2. In the dataset of UVS auroral images analyzed here, the dusk sector is brighter  
275 than the dawn sector in ~85% of the cases. Regardless of the size of the sector, the reference

276 oval in use and the assumed auroral width, the median power ratios are several times larger  
277 than unity, indicating a dusk region more powerful than the dawn one (Table 1). We note  
278 that, compared to a “generic mask” such as our MS mask, adjusting for the precise location  
279 of the main emissions (AF1 masks), and to their width (AF2 masks) tends to increase the value  
280 of the median ratio. This is because the adjusted masks better select the more variable dusk  
281 arc ( or multiple arcs). Furthermore, we note that, while the AF2 masks, being wider, may  
282 capture emissions arising from different mechanisms than the rest of the MEs, the inclusion  
283 of a larger region does not fundamentally modify the results.

284 In the B15 sector, the median ratio varies from 3.4 (MD mask) to 3.9 (AF2 mask) in the  
285 northern hemisphere, while in the southern hemisphere it varies from 4.2 (MD mask) to 5.5  
286 (AF2 mask). Thus, our results are qualitatively similar to those obtained by Bonfond et al.,  
287 2015 in the south (a median dusk/dawn ratio of 3.1).. Additionally, our values in the north  
288 are relatively similar to those in the south (3.4 compared to 4.2 for the B15 sector and the  
289 MD mask, which the combination closest to the method used in Bonfond et al. 2015). This  
290 result validates the reservations of Bonfond et al. (2015) concerning their own results in  
291 north, which they considered unreliable because they were tainted by a selection bias.  
292 Nevertheless, we note that our value in the south remains higher than the one deduced from  
293 the HST images. We attribute at least part of the difference in the results to the color ratio  
294 (CR) assumed to be constant over the main emissions in the previous study. The color ratio  
295 measures the absorption of light from the atmospheric constituents and is given by the ratio  
296 of intensity of light in an unabsorbed band (155-162 nm) and the intensity in an absorbed  
297 band (123-130 nm) (Yung et al., 1982; Gustin et al., 2012). By assuming a constant CR, they  
298 considered all the emissions to take place at the same depth. Gérard et al. (2016) have shown  
299 that the brightness and the color ratio are correlated in the main emissions. The throughput

300 of the broadband filter used for Far-UV imaging with the Space Telescope Imaging  
301 Spectrograph (STIS) and the Advanced Camera for Surveys (ACS) have a triangular shape (see  
302 Figure1 in Gustin et al. 2012), putting an emphasis on the shorter wavelengths (those  
303 absorbed by methane) Hence, for a similar initial brightness, the more absorbed emissions  
304 appear attenuated in the images. As a consequence, when the color ratio and brightness are  
305 correlated, the apparent contrast between bright and absorbed features on one hand and  
306 dim but less absorbed features on the other hand is reduced. Because the Juno-UVS  
307 observations provide spectral information between 68-210 nm, it is possible to multiply the  
308 observed spectra by the throughput of the filters used by the cameras on board HST to  
309 simulate these observations. A test applied to the southern hemisphere during PJ4 indeed  
310 showed that the use of the throughput of the HST SrF2 filter led to a ~10% decrease on the  
311 dusk/dawn ratio, compared to the unaltered UVS brightness. However, this computation  
312 assumes that HST can observe the Jovian pole from the same vantage point as Juno. Changing  
313 the elevation angle from ~30° to ~80° would further increase the CR contrast and thus  
314 decrease the dusk/dawn ratio.

315

316 Slightly lower dusk-over-dawn ratios are found in the SYM sector, with median ratios on the  
317 order of 2.9 to 4.0. We attribute this to the size of the sectors. Indeed, the SYM sector is twice  
318 larger than the B15. Thus, there are more chances for a bright patch of emission to be covered  
319 by a given mask in the SYM sector. If this patch is in the dusk region, it has a low impact on  
320 the ratio since the dusk region is generally made of bright emissions. Conversely, if the patch  
321 is in the dawn region, it can have a larger impact, which results in lowering the power ratio.  
322 Either way, we found a brighter dusk region for both sectors.

323 We computed the mean value and the variance of the emitted power in the different sectors  
324 (table S4) and we did not find that the variance is significant different in one sector compared  
325 to the other. Thus, the variability of the ratio cannot be preferentially attributed to one local  
326 time sector. The power difference between the dusk and dawn sectors could have been used  
327 as an alternative parameter (see its median values in table S3), but it would lead to the same  
328 general conclusion, with the drawback of being sensitive to the size of the sectors.

329

330 Some perijoves displayed a more powerful dawn region. This is the case for PJ3, 10, 12, 15,  
331 18, 26 and 32. Different reasons can explain this trend. First, we have found dawn storms  
332 during PJ3 and PJ32. These are not the only perijoves during which dawn storms have been  
333 observed, but the others are captured at stages where the power amplification is not yet  
334 present or significant enough to inverse the ratio. During PJ10, 12, 15 and 18, a main aurora  
335 brightening (MAB) and a compression of the main emissions are visible. This case is often  
336 coupled with a more complex morphology of the main emissions in the dusk region. Such  
337 auroral morphologies are generally associated with the arrival of a solar wind shock (Grodent  
338 et al., 2018; Nichols et al., 2007; Yao et al., 2022). Therefore, the MD and AF1 masks cannot  
339 cover the whole main emissions, and the dawn region seems more powerful with these  
340 masks. When using the AF2 mask, the dusk region can be better covered, and the power ratio  
341 goes back to a value closer to unity. No trend can be identified concerning the more powerful  
342 region in this case, as the ratios have values slightly higher or lower than unity. In the case of  
343 PJ26, the main emissions vanished in the dusk region of the northern hemisphere, which led  
344 to the dawn section being brighter than the dusk one. The three explanations for these low  
345 ratios are illustrated in Figure 3.

346

## 347 **5 | Summary and conclusion**

348

349

350 Using data gathered over the first 39 Juno perijoves, we have conducted a study of the  
351 emitted power from the dusk and dawn regions of the main emissions. To analyze the impact  
352 of the accuracy of the identification of the main emissions on the results, 3 different masks  
353 have been created to isolate the regions. The first one uses the Vogt et al. (2011) model to  
354 link the magnetospheric plasma to auroral features in order to build a “generic” mask. The  
355 second one is built specifically for each image and covers the region of highest brightness,  
356 assuming it is the main emissions. Finally, the third one is similar to the second one, but with  
357 a variable width permitted to cover the wider parts of the main emissions. In addition to these  
358 3 masks, 2 sectors have been chosen for the study. The first sector extends from 16:00 to  
359 18:00 LT in the dusk region, and from 06:00 to 08:00 LT in the dawn one, allowing for  
360 comparisons with previous results from Bonfond et al. (2015). The second sector range  
361 chosen is an extension of the first one to set it symmetrically with respect to the 18:00 LT and  
362 06:00 LT directions, i.e., 16:00 to 20:00 LT in the dusk region, and 04:00 to 08:00 LT in the  
363 dawn region. Our analyses show that, whatever the combination of mask and sector, we  
364 obtain the same results:

365

- 366 • The median dusk-over-dawn power ratios are ~3-4 times higher than unity for every  
367 hemisphere, mask and sector, indicative of a dusk region generally more powerful. We

368 note that this behavior is seen whether the dusk-side main emissions are formed of a  
369 single regular arc (e.g. PJ8 south) or display a more complex morphology.

370 • Some perijoves displayed a dawn region more powerful than the dusk one, and 3 main  
371 reasons can be evoked to explain it. There have been dawn storms during some  
372 perijoves, main auroral brightenings due to increases in the solar wind ram pressure  
373 in some others, and a surprising disappearance of the main emissions in the dusk  
374 region has been found in the northern hemisphere of PJ26.

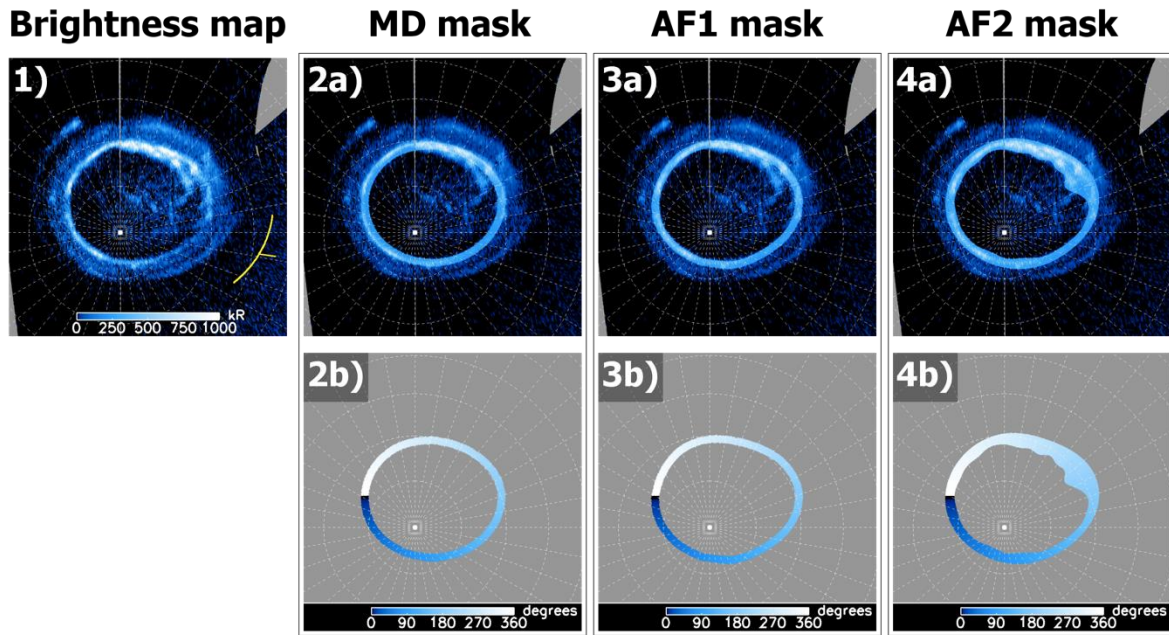
375

376 Our results are similar to those obtained by Bonfond et al. (2015) in the southern hemisphere  
377 and are still opposite to the expectations from the modeling of (Ray et al., 2014). The former  
378 suggested that, if the main emissions brightness is proportional to the field aligned currents  
379 in the middle magnetosphere, then this asymmetry could be qualitatively compatible with  
380 the combination of the upward (relative to the ionosphere) FACs related to the corotation  
381 breakdown in the middle magnetosphere and the FACs closing the partial ring currents in the  
382 ionosphere flowing downward in the dawn sector and upward in the dusk sector (aka. Region  
383 2 currents). Lorch et al. (2020) used data gathered over 39 years with 7 spacecraft to study  
384 the asymmetry in the magnetodisk currents. They found that azimuthal currents are fed at  
385 dusk and removed at dawn, in agreement with the concept of partial ring current, confirming  
386 earlier results from Khurana (2001). On the other hand, they also showed that the radial  
387 currents were weaker on the dusk side compared to the dawn side beyond 30R<sub>J</sub>. Thus,  
388 because they arise from the combination of these opposite effects, the inferred total field  
389 aligned currents do not bear a clear and unambiguous imprint of region 2 currents able to  
390 explain the auroral observations discussed here. (Nichols and Cowley, 2022) showed an

391 excellent temporal correlation between the radial currents and the auroral brightness of the  
392 MEs on the dawn side. They also concluded that the FACs related to the closure of the partial  
393 ring current in the dawn sector should be  $\sim 10$  times smaller than those associated with the  
394 drop of corotation in the middle magnetosphere ( $0.25 \mu\text{A}/\text{m}^2$  compared to  $1\text{-}3 \mu\text{A}/\text{m}^2$ ) and  
395 thus have a limited influence on the aurora. Since the dusk side has the weakest radial  
396 currents but the brightest auroral emissions, we must conclude that, despite the good  
397 temporal correlation observed on the dawn side, there is no spatial correlation between the  
398 aurora and the radial currents. Furthermore, if the closing of the partial ring current does not  
399 trigger a large auroral response, then the auroral emissions do not provide a faithful image of  
400 the field aligned currents, even in the MEs region. An alternative or supplemental explanation  
401 for the main emissions could arise from the finding of stronger plasma turbulences on the  
402 dusk side of the magnetosphere below 50 RJ compared to the dawn side (Tao et al., 2015).  
403 Indeed, other aurora triggering processes involving ultra-low frequency (ULF) waves and/or  
404 Alfvén waves have been discussed (Nichols et al., 2017b; Saur et al., 2018; Pan et al., 2021;  
405 Lorch et al., 2022; Feng et al., 2022) and their impact on the brightness and morphology of  
406 the UV auroral emissions would certainly deserve a closer exploration in a near future as the  
407 evolution of Juno's orbit now allows dawn/dusk comparisons.

408

409

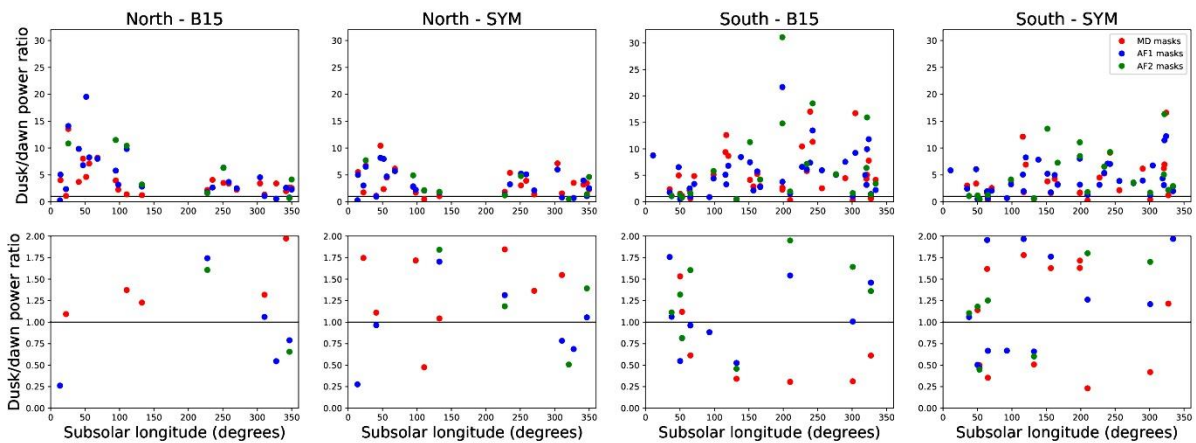


410

411 Figure 1: 1) Polar projection of the southern pole during PJ38. The sunward directions spanned over  
 412 the data used to create the map are indicated by a yellow region, with the radially extended part  
 413 referring to the mean sunward direction that has been used for the computations. For panels 2, 3 and  
 414 4, images a) are the same polar projection as panel 1 with MD, AF1 and AF2 masks respectively  
 415 added on. Images b) are polar projections of the masks alone.

416

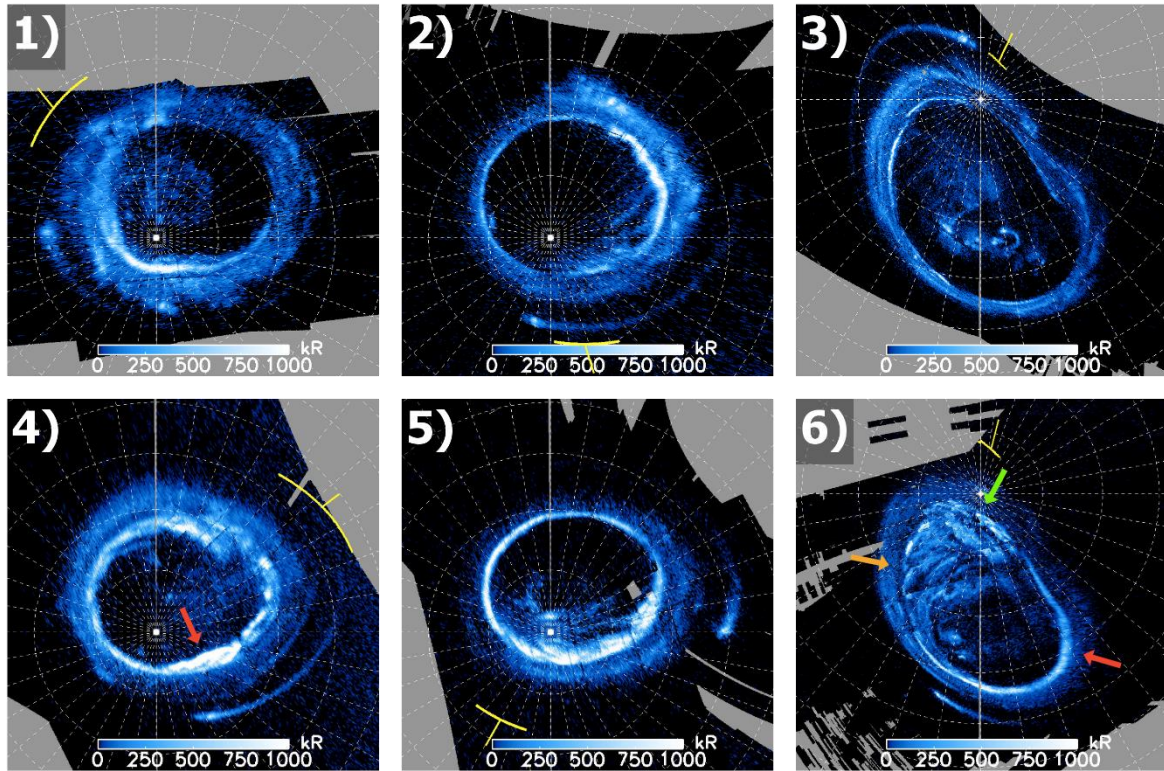
417



418

419 Figure 2: Top: dusk-over-dawn power ratios for the different sectors as a function of subsolar  
 420 longitude. Bottom: Zoomed version of the same plot, centered on the value 1. One can see that the  
 421 different methods can provide different results for individual cases, but for every method, dusk-over-  
 422 dawn ratios above 1 vastly outnumber those under 1.

423



424

425 Figure 3: Illustration of three typical cases where the dusk region is more powerful than the dawn one  
 426 (top line) and three atypical cases where the dawn region is more powerful than the dusk one (bottom  
 427 line). The yellow arc and tick mark show the orientation of the Sun during the image acquisition. 1)  
 428 Polar projection of the southern pole during PJ5. 2) Polar projection of the southern pole during PJ7.  
 429 3) Polar projection of the northern pole during PJ13. 4) Polar projection of the southern pole during  
 430 PJ32. A dawn storm is indicated by the red arrow. 5) Polar projection of the southern pole during PJ12.  
 431 An enhancement of the main emissions at all longitudes is visible. 6) Polar projection of the northern  
 432 pole during PJ26. The red arrow points toward the dawn part of the main emissions where they are  
 433 clearly visible. The green arrow points toward the noon part, where they are harder to distinguish  
 434 from the polar emissions but still recognizable. Finally, the orange arrow points toward the dusk  
 435 region, where the main emissions vanished and a strong decrease in the brightness is visible between  
 436 the polar and outer emissions. In the three images, the sunward direction is indicated the same way  
 437 as in Figure 1.

438

		B15 sector Median	SYM sector Median
MD mask	North	3.40	3.04
	South	4.24	2.92
AF1 mask	North	3.43	2.94
	South	4.73	3.22
AF2 mask	North	3.91	3.25
	South	5.47	4.04

439

440 Table 1: Median dusk-over-dawn power ratios for the MD, AF1 and AF2 masks in the southern and  
441 northern hemispheres, for both the B15 and SYM sectors.

442

## 443 **6| Acknowledgements**

444

445 We are grateful to NASA and contributing institutions which have made the Juno mission  
446 possible. B. Bonfond is a Research Associate of the Fonds de la Recherche Scientifique - FNRS.  
447 B. Bonfond, D. Grodent and J.-C. Gérard acknowledge financial support from the Belgian  
448 Federal Science Policy Office (BELSPO) via the PRODEX Programme of ESA. This work was  
449 funded by NASA's New Frontiers Program for Juno via contract with the Southwest Research  
450 Institute. VH acknowledges support from the French government under the France 2030  
451 investment plan, as part of the Initiative d'Excellence d'Aix-Marseille Université – A\*MIDEX  
452 AMX-22-CPJ-04.

453

## 454 **References**

455

456 Bolton, S.J., Lunine, J., Stevenson, D., Connerney, J.E.P., Levin, S., Owen, T.C., Bagenal, F.,  
457 Gautier, D., Ingersoll, A.P., Orton, G.S., Guillot, T., Hubbard, W., Bloxham, J., Coradini, A.,  
458 Stephens, S.K., Mokashi, P., Thorne, R., Thorpe, R., 2017. The Juno Mission. *Space Sci Rev*  
459 213, 5–37. <https://doi.org/10.1007/s11214-017-0429-6>

460 Bonfond, B., Grodent, D., Gérard, J.-C., Stallard, T., Clarke, J.T., Yoneda, M., Radioti, A.,  
461 Gustin, J., 2012. Auroral evidence of Io's control over the magnetosphere of Jupiter.  
462 *Geophysical Research Letters* 39. <https://doi.org/10.1029/2011GL050253>

463 Bonfond, B., Gustin, J., Gérard, J.-C., Grodent, D., Radioti, A., Palmaerts, B., Badman, S.V.,  
464 Khurana, K.K., Tao, C., 2015. The far-ultraviolet main auroral emission at Jupiter – Part 1:  
465 Dawn–dusk brightness asymmetries. *Annales Geophysicae* 33, 1203–1209.  
466 <https://doi.org/10.5194/angeo-33-1203-2015>

467 Bonfond, B., Yao, Z., Grodent, D., 2020. Six Pieces of Evidence Against the Corotation  
468 Enforcement Theory to Explain the Main Aurora at Jupiter. *Journal of Geophysical Research:*  
469 *Space Physics* 125, e2020JA028152. <https://doi.org/10.1029/2020JA028152>

470 Bonfond, B., Yao, Z.H., Gladstone, G.R., Grodent, D., Gérard, J.-C., Matar, J., Palmaerts, B.,  
471 Greathouse, T.K., Hue, V., Versteeg, M.H., Kammer, J.A., Giles, R.S., Tao, C., Vogt, M.F.,  
472 Mura, A., Adriani, A., Mauk, B.H., Kurth, W.S., Bolton, S.J., 2021. Are Dawn Storms Jupiter's  
473 Auroral Substorms? *AGU Advances* 2, e2020AV000275.  
474 <https://doi.org/10.1029/2020AV000275>

475 Clarke, J.T., Nichols, J., Gérard, J.-C., Grodent, D., Hansen, K.C., Kurth, W., Gladstone, G.R.,  
476 Duval, J., Wannawichian, S., Bunce, E., Cowley, S.W.H., Cray, F., Dougherty, M., Lamy, L.,

477 Mitchell, D., Pryor, W., Retherford, K., Stallard, T., Zieger, B., Zarka, P., Cecconi, B., 2009.  
478 Response of Jupiter's and Saturn's auroral activity to the solar wind. *Journal of Geophysical*  
479 *Research: Space Physics* 114. <https://doi.org/10.1029/2008JA013694>

480 Connerney, J.E.P., Kotsiaros, S., Oliverson, R.J., Espley, J.R., Joergensen, J.L., Joergensen, P.S.,  
481 Merayo, J.M.G., Herceg, M., Bloxham, J., Moore, K.M., Bolton, S.J., Levin, S.M., 2018. A New  
482 Model of Jupiter's Magnetic Field From Juno's First Nine Orbits. *Geophysical Research*  
483 *Letters* 45, 2590–2596. <https://doi.org/10.1002/2018GL077312>

484 Connerney, J.E.P., Timmins, S., Oliverson, R.J., Espley, J.R., Joergensen, J.L., Kotsiaros, S.,  
485 Joergensen, P.S., Merayo, J.M.G., Herceg, M., Bloxham, J., Moore, K.M., Mura, A., Moirano,  
486 A., Bolton, S.J., Levin, S.M., 2022. A New Model of Jupiter's Magnetic Field at the  
487 Completion of Juno's Prime Mission. *Journal of Geophysical Research: Planets* 127,  
488 e2021JE007055. <https://doi.org/10.1029/2021JE007055>

489 Cowley, S.W.H., Bunce, E.J., 2001. Origin of the main auroral oval in Jupiter's coupled  
490 magnetosphere–ionosphere system. *Planetary and Space Science, Magnetosphere of the*  
491 *Outer Planets Part II* 49, 1067–1088. [https://doi.org/10.1016/S0032-0633\(00\)00167-7](https://doi.org/10.1016/S0032-0633(00)00167-7)

492 Davis, M.W., Gladstone, G.R., Greathouse, T.K., Slater, D.C., Versteeg, M.H., Persson, K.B.,  
493 Winters, G.S., Persyn, S.C., Eterno, J.S., 2011. Radiometric performance results of the Juno  
494 ultraviolet spectrograph (Juno-UVS), in: *UV/Optical/IR Space Telescopes and Instruments:*  
495 *Innovative Technologies and Concepts V. Presented at the UV/Optical/IR Space Telescopes*  
496 *and Instruments: Innovative Technologies and Concepts V, SPIE*, pp. 42–54.  
497 <https://doi.org/10.1117/12.894274>

498 Feng, E., Zhang, B., Yao, Z., Delamere, P.A., Zheng, Z., Brambles, O.J., Ye, S.-Y., Sorathia, K.A.,  
499 2022. Dynamic Jovian Magnetosphere Responses to Enhanced Solar Wind Ram Pressure:  
500 Implications for Auroral Activities. *Geophysical Research Letters* 49, e2022GL099858.  
501 <https://doi.org/10.1029/2022GL099858>

502 Gérard, J.-C., Bonfond, B., Grodent, D., Radioti, A., 2016. The color ratio-intensity relation in  
503 the Jovian aurora: Hubble observations of auroral components. *Planetary and Space Science*  
504 131, 14–23. <https://doi.org/10.1016/j.pss.2016.06.004>

505 Gladstone, G.R., Persyn, S.C., Eterno, J.S., Walther, B.C., Slater, D.C., Davis, M.W., Versteeg,  
506 M.H., Persson, K.B., Young, M.K., Dirks, G.J., Sawka, A.O., Tumlinson, J., Sykes, H., Beshears,  
507 J., Rhoad, C.L., Cravens, J.P., Winters, G.S., Klar, R.A., Lockhart, W., Piepgrass, B.M.,  
508 Greathouse, T.K., Trantham, B.J., Wilcox, P.M., Jackson, M.W., Siegmund, O.H.W., Vallergera,  
509 J.V., Raffanti, R., Martin, A., Gérard, J.-C., Grodent, D.C., Bonfond, B., Marquet, B., Denis, F.,  
510 2017. The Ultraviolet Spectrograph on NASA's Juno Mission. *Space Sci Rev* 213, 447–473.  
511 <https://doi.org/10.1007/s11214-014-0040-z>

512 Grodent, D., 2015. A Brief Review of Ultraviolet Auroral Emissions on Giant Planets. *Space*  
513 *Sci Rev* 187, 23–50. <https://doi.org/10.1007/s11214-014-0052-8>

514 Grodent, D., Bonfond, B., Gérard, J.-C., Radioti, A., Gustin, J., Clarke, J.T., Nichols, J.,  
515 Connerney, J.E.P., 2008. Auroral evidence of a localized magnetic anomaly in Jupiter's

516 northern hemisphere. *Journal of Geophysical Research: Space Physics* 113.  
517 <https://doi.org/10.1029/2008JA013185>

518 Grodent, D., Bonfond, B., Yao, Z., Gérard, J.-C., Radioti, A., Dumont, M., Palmaerts, B.,  
519 Adriani, A., Badman, S.V., Bunce, E.J., Clarke, J.T., Connerney, J.E.P., Gladstone, G.R.,  
520 Greathouse, T., Kimura, T., Kurth, W.S., Mauk, B.H., McComas, D.J., Nichols, J.D., Orton, G.S.,  
521 Roth, L., Saur, J., Valek, P., 2018. Jupiter's Aurora Observed With HST During Juno Orbits 3 to  
522 7. *Journal of Geophysical Research: Space Physics* 123, 3299–3319.  
523 <https://doi.org/10.1002/2017JA025046>

524 Gustin, J., Bonfond, B., Grodent, D., Gérard, J.-C., 2012. Conversion from HST ACS and STIS  
525 auroral counts into brightness, precipitated power, and radiated power for H2 giant planets.  
526 *Journal of Geophysical Research: Space Physics* 117. <https://doi.org/10.1029/2012JA017607>

527 Hill, T.W., 2001. The Jovian auroral oval. *J. Geophys. Res.* 106, 8101–8108.  
528 <https://doi.org/10.1029/2000JA000302>

529 Hue, V., Giles, R.S., Gladstone, G.R., Greathouse, T.K., Davis, M.W., Kammer, J.A., Versteeg,  
530 M.H., 2021. Updated radiometric and wavelength calibration of the Juno ultraviolet  
531 spectrograph. *Journal of Astronomical Telescopes, Instruments, and Systems* 7, 044003.  
532 <https://doi.org/10.1117/1.JATIS.7.4.044003>

533 Hue, V., Gladstone, G.R., Greathouse, T.K., Kammer, J.A., Davis, M.W., Bonfond, B.,  
534 Versteeg, M.H., Grodent, D.C., Gérard, J.-C., Bolton, S.J., Levin, S.M., Byron, B.D., 2019. In-  
535 flight Characterization and Calibration of the Juno-ultraviolet Spectrograph (Juno-UVS). *The*  
536 *Astronomical Journal* 157, 90. <https://doi.org/10.3847/1538-3881/aafb36>

537 Kamran, A., Bunce, E.J., Cowley, S.W.H., James, M.K., Nichols, J.D., Provan, G., Cao, H., Hue,  
538 V., Greathouse, T.K., Gladstone, G.R., 2022. Auroral Field-Aligned Current Signatures in  
539 Jupiter's Magnetosphere: Juno Magnetic Field Observations and Physical Modeling. *Journal*  
540 *of Geophysical Research: Space Physics* 127, e2022JA030431.  
541 <https://doi.org/10.1029/2022JA030431>

542 Khurana, K.K., 2001. Influence of solar wind on Jupiter's magnetosphere deduced from  
543 currents in the equatorial plane. *Journal of Geophysical Research: Space Physics* 106,  
544 25999–26016. <https://doi.org/10.1029/2000JA000352>

545 Kotsiaros, S., Connerney, J.E.P., Clark, G., Allegrini, F., Gladstone, G.R., Kurth, W.S., Mauk,  
546 B.H., Saur, J., Bunce, E.J., Gershman, D.J., Martos, Y.M., Greathouse, T.K., Bolton, S.J., Levin,  
547 S.M., 2019. Birkeland currents in Jupiter's magnetosphere observed by the polar-orbiting  
548 Juno spacecraft. *Nat Astron* 3, 904–909. <https://doi.org/10.1038/s41550-019-0819-7>

549 Lorch, C.T.S., Ray, L.C., Arridge, C.S., Khurana, K.K., Martin, C.J., Bader, A., 2020. Local Time  
550 Asymmetries in Jupiter's Magnetodisc Currents. *Journal of Geophysical Research: Space*  
551 *Physics* 125, e2019JA027455. <https://doi.org/10.1029/2019JA027455>

552 Lorch, C.T.S., Ray, L.C., Wilson, R.J., Bagenal, F., Cray, F., Delamere, P.A., Damiano, P.A.,  
553 Watt, C.E.J., Allegrini, F., 2022. Evidence of Alfvénic Activity in Jupiter's Mid-To-High Latitude

554 Magnetosphere. *Journal of Geophysical Research: Space Physics* 127, e2021JA029853.  
555 <https://doi.org/10.1029/2021JA029853>

556 Nichols, J.D., Badman, S.V., Bagenal, F., Bolton, S.J., Bonfond, B., Bunce, E.J., Clarke, J.T.,  
557 Connerney, J.E.P., Cowley, S.W.H., Ebert, R.W., Fujimoto, M., Gérard, J.-C., Gladstone, G.R.,  
558 Grodent, D., Kimura, T., Kurth, W.S., Mauk, B.H., Murakami, G., McComas, D.J., Orton, G.S.,  
559 Radioti, A., Stallard, T.S., Tao, C., Valek, P.W., Wilson, R.J., Yamazaki, A., Yoshikawa, I.,  
560 2017a. Response of Jupiter's auroras to conditions in the interplanetary medium as  
561 measured by the Hubble Space Telescope and Juno. *Geophysical Research Letters* 44, 7643–  
562 7652. <https://doi.org/10.1002/2017GL073029>

563 Nichols, J.D., Bunce, E.J., Clarke, J.T., Cowley, S.W.H., Gérard, J.-C., Grodent, D., Pryor, W.R.,  
564 2007. Response of Jupiter's UV auroras to interplanetary conditions as observed by the  
565 Hubble Space Telescope during the Cassini flyby campaign. *Journal of Geophysical Research:*  
566 *Space Physics* 112. <https://doi.org/10.1029/2006JA012005>

567 Nichols, J.D., Clarke, J.T., Gérard, J.C., Grodent, D., Hansen, K.C., 2009. Variation of different  
568 components of Jupiter's auroral emission. *Journal of Geophysical Research: Space Physics*  
569 114. <https://doi.org/10.1029/2009JA014051>

570 Nichols, J.D., Cowley, S.W.H., 2022. Relation of Jupiter's Dawnside Main Emission Intensity  
571 to Magnetospheric Currents During the Juno Mission. *Journal of Geophysical Research:*  
572 *Space Physics* 127, e2021JA030040. <https://doi.org/10.1029/2021JA030040>

573 Nichols, J.D., Yeoman, T.K., Bunce, E.J., Chowdhury, M.N., Cowley, S.W.H., Robinson, T.R.,  
574 2017b. Periodic Emission Within Jupiter's Main Auroral Oval. *Geophysical Research Letters*  
575 44, 9192–9198. <https://doi.org/10.1002/2017GL074824>

576 Pan, D.-X., Yao, Z.-H., Manners, H., Dunn, W., Bonfond, B., Grodent, D., Zhang, B.-Z., Guo, R.-  
577 L., Wei, Y., 2021. Ultralow-Frequency Waves in Driving Jovian Aurorae Revealed by  
578 Observations From HST and Juno. *Geophysical Research Letters* 48, e2020GL091579.  
579 <https://doi.org/10.1029/2020GL091579>

580 Radioti, A., Gérard, J.-C., Grodent, D., Bonfond, B., Krupp, N., Woch, J., 2008. Discontinuity in  
581 Jupiter's main auroral oval. *Journal of Geophysical Research: Space Physics* 113.  
582 <https://doi.org/10.1029/2007JA012610>

583 Ray, L.C., Achilleos, N.A., Vogt, M.F., Yates, J.N., 2014. Local time variations in Jupiter's  
584 magnetosphere-ionosphere coupling system. *Journal of Geophysical Research: Space*  
585 *Physics* 119, 4740–4751. <https://doi.org/10.1002/2014JA019941>

586 Saur, J., Janser, S., Schreiner, A., Clark, G., Mauk, B.H., Kollmann, P., Ebert, R.W., Allegrini, F.,  
587 Szalay, J.R., Kotsiaros, S., 2018. Wave-Particle Interaction of Alfvén Waves in Jupiter's  
588 Magnetosphere: Auroral and Magnetospheric Particle Acceleration. *Journal of Geophysical*  
589 *Research: Space Physics* 123, 9560–9573. <https://doi.org/10.1029/2018JA025948>

590 Sulaiman, A.H., Mauk, B.H., Szalay, J.R., Allegrini, F., Clark, G., Gladstone, G.R., Kotsiaros, S.,  
591 Kurth, W.S., Bagenal, F., Bonfond, B., Connerney, J.E.P., Ebert, R.W., Elliott, S.S., Gershman,  
592 D.J., Hospodarsky, G.B., Hue, V., Lysak, R.L., Masters, A., Santolík, O., Saur, J., Bolton, S.J.,

593 2022. Jupiter's Low-Altitude Auroral Zones: Fields, Particles, Plasma Waves, and Density  
594 Depletions. *Journal of Geophysical Research: Space Physics* 127, e2022JA030334.  
595 <https://doi.org/10.1029/2022JA030334>

596 Tao, C., Sahraoui, F., Fontaine, D., de Patoul, J., Chust, T., Kasahara, S., Retinò, A., 2015.  
597 Properties of Jupiter's magnetospheric turbulence observed by the Galileo spacecraft.  
598 *Journal of Geophysical Research: Space Physics* 120, 2477–2493.  
599 <https://doi.org/10.1002/2014JA020749>

600 Vogt, M.F., Kivelson, M.G., Khurana, K.K., Walker, R.J., Bonfond, B., Grodent, D., Radioti, A.,  
601 2011. Improved mapping of Jupiter's auroral features to magnetospheric sources. *Journal of*  
602 *Geophysical Research: Space Physics* 116. <https://doi.org/10.1029/2010JA016148>

603 Yao, Z.H., Bonfond, B., Grodent, D., Chané, E., Dunn, W.R., Kurth, W.S., Connerney, J.E.P.,  
604 Nichols, J.D., Palmaerts, B., Guo, R.L., Hospodarsky, G.B., Mauk, B.H., Kimura, T., Bolton, S.J.,  
605 2022. On the Relation Between Auroral Morphologies and Compression Conditions of  
606 Jupiter's Magnetopause: Observations From Juno and the Hubble Space Telescope. *Journal*  
607 *of Geophysical Research: Space Physics* 127, e2021JA029894.  
608 <https://doi.org/10.1029/2021JA029894>

609 Yung, Y.L., Gladstone, G.R., Chang, K.M., Ajello, J.M., Srivastava, S.K., 1982. H<sub>2</sub> fluorescence  
610 spectrum from 1200 to 1700 Å by electron impact - Laboratory study and application to  
611 Jovian aurora. *The Astrophysical Journal* 254, L65–L69. <https://doi.org/10.1086/183757>

612

613